Design of All-Oxide Multilayers with High-Temperature Stability Toward Future Thermophotovoltaic Applications

Jiawei Song, Zihao He, Chao Shen, Jie Zhu, Zhimin Qi, Xing Sun, Yizhi Zhang, Juncheng Liu, Xinghang Zhang, Xiulin Ruan, Peter Bermel, and Haiyan Wang*

Thermophotovoltaic (TPV) technology converts heat into electricity using thermal radiation. Increasing operating temperature is a highly effective approach to improving the efficiency of TPV systems. However, most reported TPV selective emitters degrade rapidly via. oxidation as operating temperatures increase. To address this issue, replacing nanostructured oxide-metal films with oxide–oxide films is a promising way to greatly limit oxidation, even under high-temperature conditions. This study introduces new all-oxide photonic crystal designs for high-temperature stable TPV systems, overcoming limitations of metal phases and offering promising material choices. The designs utilize both yttria-stabilized zirconia (YSZ)/MgO and CeO_2/MgO combinations with a multilayer structure and stable high-quality growth. Both designs exhibit positive optical dielectric constants with tunable reflectivity, measured via optical characterization. Thermal stability testing using in situ heating X-ray diffraction (XRD) suggests high-temperature stability (up to 1000 °C) of both YSZ/MgO and CeO_2/MgO systems. The results demonstrate a new and promising approach to improve the high-temperature stability of TPV systems, which can be extended to a wide range of material selection and potential designs.

J. Song, C. Shen, Z. Qi, X. Sun, Y. Zhang, J. Liu, X. Zhang, H. Wang
School of Materials Engineering
Purdue University
West Lafayette, IN 47907, USA
E-mail: hwang00@purdue.edu
Z. He, J. Zhu, P. Bermel, H. Wang
Birck Nanotechnology Center and School of Electrical
and Computer Engineering
Purdue University
West Lafayette, IN 47907, USA
X. Ruan
School of Mechanical Engineering
Purdue University
West Lafayette, IN 47907, USA

1. Introduction

Thermophotovoltaic (TPV) energy conversion is a technology that converts heat into electricity through thermal radiation. A TPV system is typically composed of a heat source, a thermal emitter, and a photovoltaic (PV) cell.[1,2] Several strategies have been proposed to enhance the efficiency of TPV devices, such as utilizing multijunction cells to efficiently convert distinct regions of the electromagnetic spectrum, employing low-pass filters and reflectors to enhance radiation conversion efficiency,[3] and enhancing the performance of micro combustors.[4–6] Furthermore, using selective emitters, which have high emissivity in narrow wavelength regions, is another approach to greatly increase TPV efficiency.[7,8] Unlike broadband emitters, selective emitters utilize materials or structures that selectively transmit, reflect, or absorb light, resulting in thermal spectral emission selectivity. Selective emitters are divided into two broad categories, which include rare-earth materials and photonic crystals (PhCs).[9] Rare-earth materials display intrinsic spectral selectivity and their selective peak wavelength cannot be tuned. PhCs, on the other hand, offer more flexible emissivity spectra by tuning the materials and microstructure.[10,11]

PhCs are periodic structured materials with different dielectric constants (e.g., metals and oxides). Tungsten (W),[12–16] Tantalum (Ta),[17–20] Platinum (Pt),[21] Molybdenum (Mo),[22] and Silicon (Si)[21,23,24] are commonly used metals or semimetals in PhCs. HfO_2, Al_2O_3, WO_x, and MoO_x are commonly used oxides in PhCs. According to the Stefan–Boltzmann law, the high radiative power of an emitter requires a high operating temperature. Using refractory materials (i.e., W, Mo, Ta, HfO_2, Al_2O_3) with high melting temperatures has been proven to be a promising approach to improve high-temperature stability.[8,25–27] However, refractory metals are prone to oxidation during high-temperature conditions, which is one of the key failure mechanisms observed in structured selective emitters.[13,28,29] Since oxygen can originate from the external environment or the oxide phase in PhCs, the high-temperature stability of PhCs can be further improved by reducing oxygen in the environment (i.e., high vacuum or inert gas environment)[13,28] and limiting oxygen diffusion

**ADVANCED
SCIENCE NEWS**

www.advancedsciencenews.com

**ADVANCED
MATERIALS
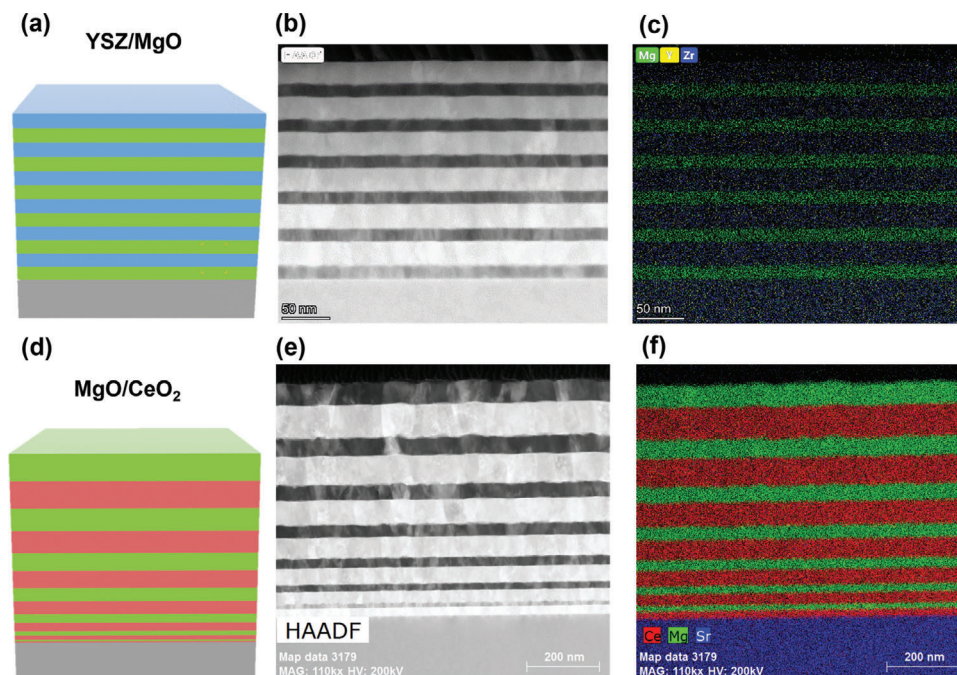INTERFACES**
Open Access

www.advmatinterfaces.de

Figure 1. Microstructure of the all-oxide multilayer designs. a) Schematic illustration of the YSZ/MgO multilayer film with equal-thickness structure; b) cross-sectional STEM image; c) EDS mapping of YSZ/MgO multilayer; d) schematic illustration of the CeO₂/MgO multilayer film with gradient-thickness structure; e) cross-sectional STEM image and (f) EDS mapping of CeO₂/MgO multilayer.

(i.e., applying protective layer, improving film quality).[30,31] Besides oxidation, structure degradation can also result from grain growth, surface diffusion, and thermal expansion.[8,32]

Considering the limitations of metal phases in PhCs under high-temperature environments, exploring all-ceramic emitter designs is a promising way to improve thermal stability from a material perspective. In this study, we introduce two new oxide-oxide 1D multilayer PhCs designs (i.e., Yttria-stabilized zirconia (YSZ)/MgO, CeO_2/MgO) and investigate their thermal stability and optical properties. YSZ, CeO_2, and MgO were selected in this study due to the following reasons. First, YSZ, CeO_2, and MgO exhibit excellent thermal stability; their melting temperatures are 2700, 2340, and 2852 °C, respectively. Second, the refractive indices of these three materials are different, which can provide periodic variations of refractive index using multilayer designs. In addition, the thermal expansion coefficients (CTE) of these three materials are comparable, and therefore the thermally induced delamination can be mitigated. A summary of the thermal parameters of YSZ, CeO_2 and MgO can be found in Table S1 (Supporting Information). X-ray diffraction (XRD) and transmission electron microscopy (TEM) analysis have been conducted to examine the microstructure of the two oxide–oxide multilayer designs. Transmittance and ellipsometry measurements have been carried out to explore the optical properties. The in situ heating XRD demonstrated that both designs are structurally stable up to 1000 °C. The new oxide–oxide PhCs designs provide a wide selection of material candidates beyond traditional metal–oxide PhCs, offering a new pathway toward high-temperature stable TPV systems.

2. Results and Discussion

Two sets of oxide–oxide multilayer films were fabricated using pulsed laser deposition (PLD): (YSZ/MgO)*6 with 6 layers of YSZ and 6 layers of MgO, (CeO_2/MgO)*7 with 7 layers of CeO_2 and 7 layers of MgO. The structure was initially designed as equal-thickness multilayers for the YSZ/MgO sample, whereas a gradient-thickness structure was implemented for the CeO_2/MgO sample to attain enhanced reflectivity across a broader frequency range. The thickness of each layer can be precisely controlled by the number of laser pulses during the deposition process, resulting in either the equal-thickness (**Figure 1a**) or the gradient-thickness (Figure 1d) structure. The X-ray diffraction analysis (XRD) suggests both two films exhibit textured growth as shown in Figure S1 (Supporting Information). More specifically, both YSZ and MgO phases show preferred (111), (200) growth orientations in YSZ/MgO multilayer film, while the CeO_2 phase exhibits (111), (200), (311) growth orientations and MgO grows along (200), (220) in the CeO_2/MgO multilayer film. The detailed microstructure was characterized by (scanning) transmission electron microscopy (TEM/STEM) coupled with energy-dispersive X-ray spectroscopy (EDS) elemental mapping. As shown in Figure 1b, the cross-sectional STEM image of YSZ/MgO multilayer film exhibits an equal-thickness structure on top of YSZ substrate. Since the contrast is proportional to the atomic number (i.e., ≈$Z^{1.7}$),[33–35] the YSZ phase (Z_{Zr} = 40, Z_Y = 39) is brighter than the MgO phase (Z_{Mg} = 12). This contrast difference suggests an alternative growth of YSZ and MgO, which can be further confirmed by the element mapping in Figure 1c. Similarly, the cross-sectional STEM images with
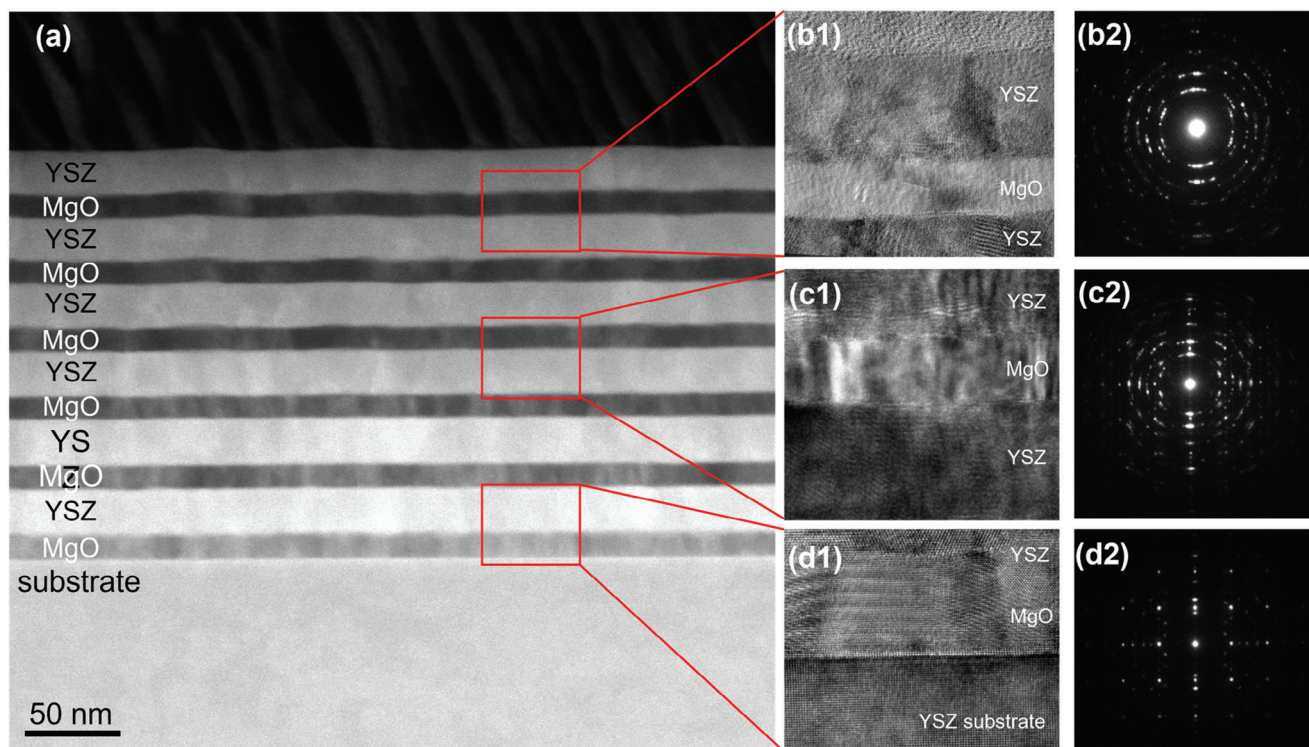
ADVANCED
SCIENCE NEWS

www.advancedsciencenews.com

**ADVANCED
MATERIALS
INTERFACES**
Open Access

www.advmatinterfaces.de

Figure 2. Detailed microstructure of YSZ/MgO multilayer film. a) Low-magnification cross-sectional STEM image; b1) high-magnification TEM image with (b2) the corresponding FFT patterns of the top area; c1) high-resolution TEM image with (c2) the corresponding FFT patterns of the middle area; d1) high-resolution TEM image with (d2) the corresponding FFT patterns of the bottom area.

corresponding EDS mapping in Figure 1e,f reveal the multilayer stacking of CeO_2 and MgO layer with gradient thickness from substrate to film surface.

To further explore the crystallinity of the films, YSZ/MgO film (as illustrated in **Figure 2**a) has been selected for detailed microstructure characterizations. Figure 2b1–d1 presents the high-magnification STEM images of three selected areas of the film, i.e., bottom (Figure 2d1), middle (Figure 2c1), and top (Figure 2b1). Well-defined and distinct interfaces indicate an abrupt change in material composition from one layer to another, without obvious interdiffusion between the two materials. Such sharp interfaces are maintained throughout the entire film, indicating a high growth quality of the multilayered film. The selected area electron diffraction (SAED) patterns taken in the cross-section <100> zone axis of the three areas of the film is shown in Figure 2b2–d2. The bottom layers exhibit an epitaxial growth relationship with the YSZ substrate as well as good crystallinity of the film, while the top layers tend to be polycrystalline when the film grows thicker. This polycrystalline growth is mainly due to the relatively large lattice mismatch between the adjacent layers ($\alpha_{YSZ} = 5.143$ Å, $\alpha_{MgO} = 4.2$ Å) as well as large film thickness.

The optical response is essential for characterizing the all-oxide multilayered design in TPV applications. To investigate the optical behavior of the YSZ/MgO and CeO_2/MgO films, angular-dependent ellipsometry measurements were performed. The dielectric permittivity values were obtained by fitting ellipsometry data with a general oscillator model and plotted in **Figure 3**b,e

for YSZ/MgO and CeO_2/MgO films, respectively. Due to the anisotropic nature of the multilayer structure, a uniaxial model ($\epsilon_\parallel \neq \epsilon_\perp$) was applied during the fitting process. As shown in Figure 3b,e, both YSZ/MgO and CeO_2/MgO designs exhibit a normal dielectric behavior because of the dielectric optical properties of YSZ, CeO_2 and MgO. Interestingly, a significant difference between the in-plane (IP) and out-of-plane (OP) permittivity in YSZ/MgO structure can be observed, whereas the CeO_2/MgO design shows similar IP and OP permittivity. In addition, angular dependent reflectivity was measured on both films (Figure 3c,f) with incident angles of 55°, 65°, and 75°. They exhibit similar characteristics that are typical of hierarchical structures, with some Fabry-Perot oscillations arising from stacking two different materials. It is worth mentioning that the CeO_2/MgO film displays more absorption peaks compared to the YSZ/MgO film, indicating that the optical properties can be tuned by altering the materials combination or layered structure (i.e., equal thickness or gradient thickness).

To test the thermal stability of the all-oxide PhCs designs, in situ XRD heating measurements were conducted under atmospheric pressure. XRD $\theta-2\theta$ scans were collected during one complete heating-cooling cycle from room temperature to 1000 °C. As shown in **Figure 4**, both YSZ/MgO and CeO_2/MgO films maintained good crystallinity, with no new peaks or disappeared peaks observed during the heating and cooling process. The peaks in the range of 32° to 38° are from the heating stage and can be neglected in subsequent analysis. During the heating process, YSZ (111) peak in Figure 4a exhibits a left
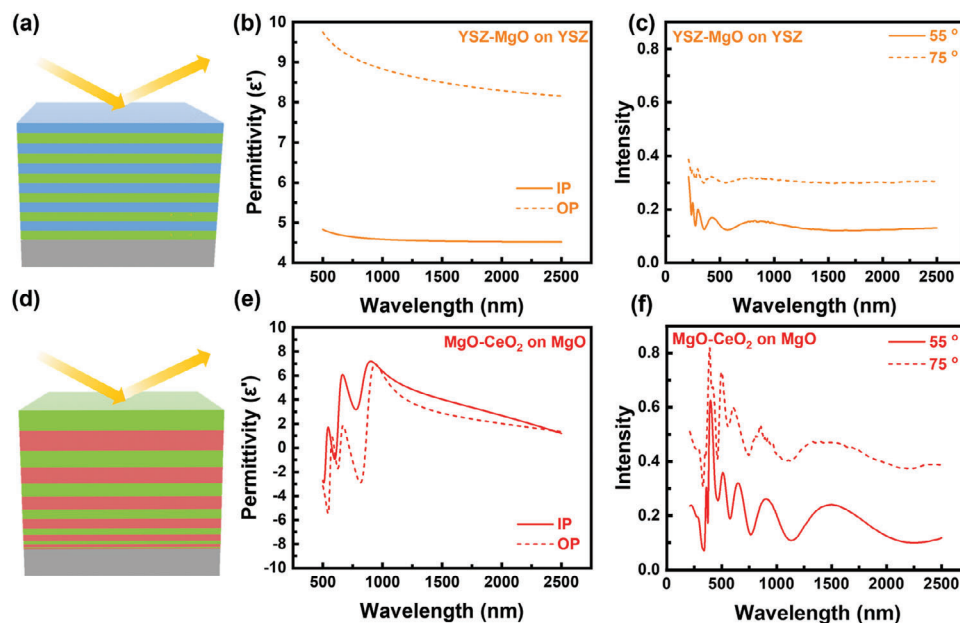
2300733 (3 of 7)

**ADVANCED
SCIENCE NEWS**

www.advancedsciencenews.com

**ADVANCED
MATERIALS
INTERFACES**
Open Access

www.advmatinterfaces.de

Figure 3. Optical properties of the all-oxide multilayer designs. a) Schematic illustration of the ellipsometry measurements on the YSZ/MgO film; b) real-part in-plane and out-of-plane dielectric constant of the YSZ/MgO film; c) angle-dependent reflectivity of the YSZ/MgO film; d) schematic illustration of the ellipsometry measurements on the CeO$_2$/MgO film; e) real-part in-plane and out-of-plane dielectric constant of the CeO$_2$/MgO film; f) angle-dependent reflectivity of the CeO$_2$/MgO film.

shift from 29.3° to 29.2°, corresponding to 3.35% thermal expansion of lattices. Similar peak shifting related to thermal expansion has been observed in YSZ (200) and MgO (200) peaks. Ideally, thermal expansion-driven peak shifting can be completely recovered after cooling. However, YSZ (111) does not return to its original peak position, instead showing a 1.64% shrinkage after the cooling process, suggesting potential strain relaxation during the heating-cooling cycle. Similar lattice expansion and peak shifting has been observed in the CeO$_2$/MgO system (Figure 4b). In addition, the photos taken on both two samples before and after the heating-cooling cycle (Figure S2, Supporting Information) suggest the multilayer films remain structurally stable without any thermally induced delamination. The CeO$_2$/MgO sample

was selected to perform an extreme heat treatment (1500 °C for 1 h.). The photos in Figure S3a,e (Supporting Information) reveal an obvious change of the sample surface, from a highly reflective surface to a non-reflective state., which suggests microstructure modification. STEM and EDS images in Figure S3 (Supporting Information) show that the layered structure has been altered by 1500 °C heat treatment while the two phases are still well separated. Considering the samples with 1000 °C heat treatment still remains their highly reflective surfaces (as shown in Figure S2, Supporting Information), the microstructure was believed still maintain its layered structure, indicating both designs (YSZ/MgO and CeO$_2$/MgO) exhibit good thermal stability up to 1000 °C.
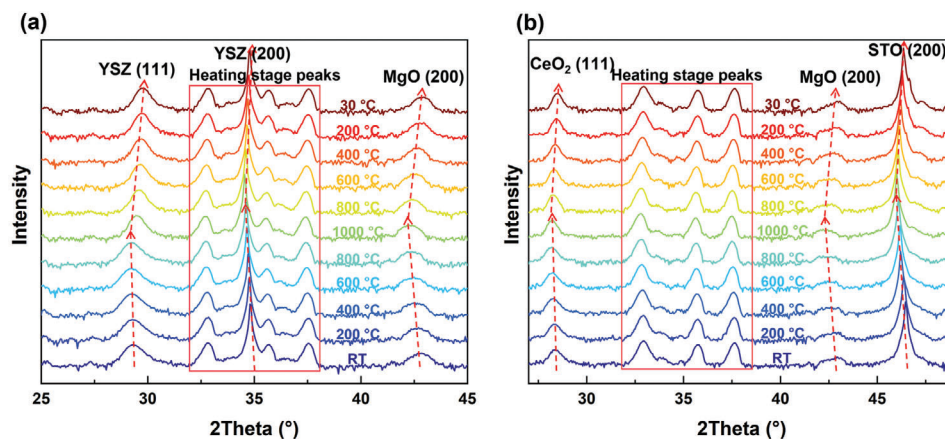

Figure 4. In situ heating XRD of the all-oxide multilayers. Stacked $\theta-2\theta$ scans of the heating–cooling cycle (RT to 1000 °C, 1000 °C to RT at ambient atmosphere): a) YSZ/MgO; b) CeO$_2$/MgO multilayers.

2300733 (4 of 7)

ADVANCED
SCIENCE NEWS

www.advancedsciencenews.com

ADVANCED
MATERIALS
INTERFACES
Open Access
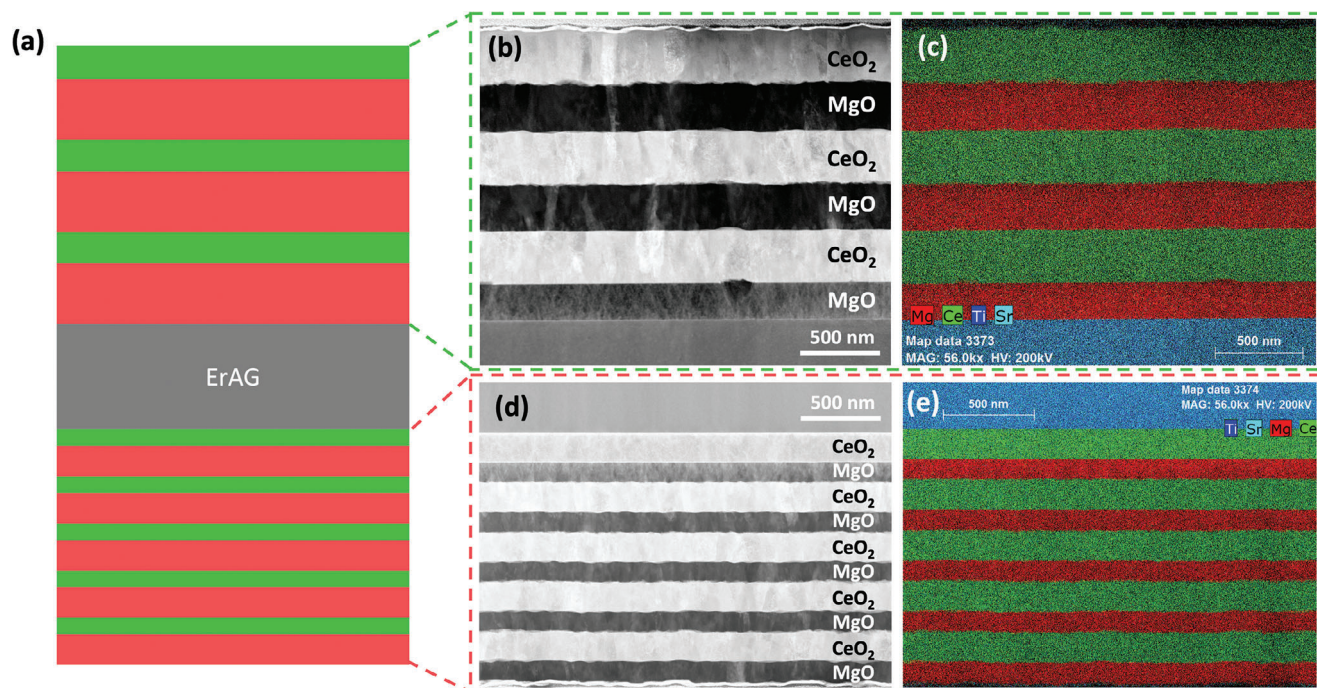
www.advmatinterfaces.de

Figure 5. TPV system using all-oxide stacking layers. a) Schematic illustration of TPV system with CeO$_2$/MgO multilayers on ErAG substrate; b) cross-sectional STEM image with (c) corresponding EDS mapping of the top films. d) Cross-sectional STEM image with (e) corresponding EDS mapping of the bottom film.

To demonstrate the relevance of these emitters to practical applications, we consider that a TPV system working at 1573 K has a peak blackbody emission value at 1.84 μm. To select a PV cell bandgap approximately matched to that emission, an arsenide-doped GaSb PV cell with a bandgap energy of ≈0.75 eV (1.65 μm) is proposed.[36,37] Considering that rare-earth emitters have narrow emission peaks in the IR region, Erbium-doped Aluminum Garnet (ErAG) is chosen as the substrate to achieve selective emission and reasonable tolerance for oxidizing environments.[8,38] The PV cell is assumed to be positioned on the top side of the emitter. To suppress long-wavelength emission to the PV cell that degrades the performance, a quarter-wave stack with reflection centered at 2.5 μm is used as the top dielectric mirror. The mirror consists of alternating layers of high- and low-index materials, in this case, CeO$_2$ and MgO. The thickness of high-index material layer is $d_H = \lambda/4n_H$, and the thickness of low-index material layer is $d_L = \lambda/4n_L$, where n_H and n_L are the refractive indices of CeO$_2$ and MgO at 2.5 μm, respectively. Further improvement can be made by constructing an exponentially chirped multilayer structure to achieve a wide band of strong reflection.[39] On the bottom side of the TPV cell, a quarter-wave stack with reflection centered at 1.47 μm is used to minimize waste energy. A schematic illustration of this TPV cell is described in **Figure 5**a and a detailed structure design with layer thickness can be found in Figure S4 (Supporting Information). Following this TPV cell design, two CeO$_2$/MgO multilayer films were deposited on both top and bottom side of ErAG substrate, and the microstructure of the films were characterized by STEM with EDS mapping. As shown in Figure 5, both sides exhibit multilayer structures as designed, with very sharp and chemically clean interfaces. The thermal stability was investigated by

XRD with in situ heating throughout one heating cycle; the results can be found in Figure S5 (Supporting Information). The thermal stability test suggests very robust phase stability of all-oxide multilayer designs, which highlights their potential uses in high-temperature TPV. Increasing operating temperature and adding cold-side filters can further enhance the efficiency of a TPV system (see Figure S6, Supporting Information). Note that since cold-side filters typically are not placed in high-temperature environments, the material choice is more relaxed. Nonetheless, tolerance for temperature cycling can be beneficial in real-world TPV experiments given the potential source temperatures, especially at pressures exceeding ultra-high vacuum conditions.

All-oxide multilayer design offers several advantages for improving the operating temperature of TPV systems. Compared to metals, refractory oxides with ultra-high melting temperatures are ideal for enhancing thermal stability while avoiding oxidation issues associated with metals. Additionally, most refractory oxides have similar thermal expansion coefficients, which help minimize structure degradation due to thermally induced delamination. This study has demonstrated two all-oxide multilayer designs with tunable optical response and high-temperature stability. This all-oxide design can be extended to various selections of refractory oxides, such as BaZrO$_3$, SrTiO$_3$, Y$_3$Al$_5$O$_{12}$, etc. Beyond oxides, refractory nitrides with high-temperature stability, and, mechanical and chemical stability, could also be considered as potential candidates in high-temperature layered emitter design. Future studies could focus on designing other nanostructures beyond multilayer including triphase or vertically-aligned nanostructures,[40–42] exploring the spectral efficiency of all-oxide TPV systems, and investigating structural stability in temperatures higher than 1000 °C and/or for longer testing periods.

**ADVANCED
SCIENCE NEWS**

www.advancedsciencenews.com

**ADVANCED
MATERIALS
INTERFACES**
Open Access

www.advmatinterfaces.de

Overall, our results highlight the potential of all-oxide multilayer structures for efficient TPV selective emitters and provide insights into the design and optimization of refractory oxide materials for a broader range of high-temperature applications.

3. Conclusion

In conclusion, our work demonstrates the potential of multilayered all-oxide designs for future high-temperature TPV applications. Two material systems have been investigated, i.e., YSZ/MgO and MgO/CeO$_2$, both with equal-thickness and graded-thickness structures. The layered structure was achieved by alternatively depositing two materials by pulsed laser deposition (PLD), and the thickness of each layer was precisely controlled by the number of laser pulses. Highly textured growth was revealed by X-ray diffraction analysis and detailed microstructure analysis shows high-quality growth with clean and very sharp interfaces. The optical characterization revealed the dielectric optical properties and the tunable reflectivity of both designs. Promising thermal stability results suggest that both designs exhibited reasonable thermal stability measured up to 1000 °C. Additionally, a TPV cell test structure was designed by depositing two CeO$_2$/MgO films on both sides of a double-side polished ErAG substrate, demonstrating the feasibility of integrating these all-oxide designs. Overall, these innovative all-oxide designs realize excellent thermal stability by incorporating refractory oxides which avoid the typical failure mechanisms in PhCs, e.g., oxidation, diffusion, and delamination. This work opens up a new direction for highly efficient, high-temperature-tolerant, experimentally relevant TPV systems.

4. Experimental Section

Thin Film Growth: The YSZ/MgO multilayer thin film was deposited on YSZ(001) substrates by alternative ablation of YSZ and MgO targets, using pulsed laser deposition (PLD) method with a KrF excimer laser (Lambda Physik Compex Pro 205, $\lambda = 248$ nm). Similarly, the CeO$_2$/MgO multilayer thin film was deposited on MgO(001) substrates by alternative ablation of CeO$_2$ and MgO targets. Before deposition, the chamber was pumped down to a high vacuum condition (2.0×10^{-6} mbar). During deposition, the substrates were heated and kept at 600 °C and 20 mTorr O$_2$ partial pressure was induced to minimize oxygen vacancy. After deposition, the chamber was naturally cooled down to room temperature in 20 mTorr O$_2$ environments.

Structural Characterization: The crystallinity was characterized by X-ray diffraction (XRD, Panalytical X'Pert X-ray diffractometer with a Cu Kα1 radiation source, $\lambda = 0.15406$ nm). The microstructure of the films was investigated by TEM (FEI TALOS 200X operated at 200 kV). TEM samples were prepared by standard manual grinding, dimpling and ion milling process.

Optical Characterization: Angular-dependent ellipsometry measurements were conducted by using a RC2 spectroscopic ellipsometer (J.A. Woollam Company). The dielectric constants were retrieved by fitting the ellipsometry data in CompleteEase software.

Supporting Information

Supporting Information is available from the Wiley Online Library or from the author.

Conflict of Interest

The authors declare no conflict of interest.

Data Availability Statement

The data that support the findings of this study are available in the supplementary material of this article.

[1] R. Sakakibara, V. Stelmakh, W. R. Chan, M. Ghebrebrhan, J. D. Joannopoulos, M. Soljacic, I. Celanovic, *J Photonics Energy* **2019**, *9*, 32713.

[2] M. M. A. Gamel, H. J. Lee, W. E. S. W. A. Rashid, P. J. Ker, L. K. Yau, M. A. Hannan, M. Z. Jamaludin, Z. Jamaludin, *Materials* **2021**, *14*, 4944.

[3] E. Nefzaoui, J. Drevillon, K. Joulain, *J. Appl. Phys.* **2012**, *111*, 084316.

[4] W. Zuo, Z. Chen, J. E., Q. Li, G. Zhang, Y. Huang, *Energy* **2023**, *266*, 126434.

[5] W. Zuo, D. Li, J. E., Y. Xia, Q. Li, Y. Quan, G. Zhang, *Energy* **2023**, *263*, 126028.

[6] W. Zuo, Z. Wang, J. E., Q. Li, Q. Cheng, Y. Wu, K. Zhou, *Energy* **2023**, *263*, 125957.

[7] N. A. Pfiester, T. E. Vandervelde, *Phys. Status Solidi. (A) Appl. Mater. Sci.* **2017**, *214*, 1600410.

[8] Z. Wang, D. Kortge, Z. He, J. Song, J. Zhu, C. Lee, H. Wang, P. Bermel, *Sol. Energy Mater. Sol. Cells* **2022**, *238*, 111554.

[9] P. Bermel, J. Lee, J. D. Joannopoulos, I. Celanovic, M. Soljačie, S. Soljačie, *Nano Lett.* **2012**, *15*, 231.

[10] D. Diso, A. Licciulli, A. Bianco, G. Leo, G. Torsello, S. Tundo, A. De Risi, M. Mazzer, presented at *AIP Conf. Proc.*, Rome (Italy), September, **2002**, *653*, pp. 132–141.

[11] R. Bhatt, I. Kravchenko, M. Gupta, *Sol. Energy* **2020**, *197*, 538.

[12] C.-C. Chang, W. J. M. Kort-Kamp, J. Nogan, T. S. Luk, A. K. Azad, A. J. Taylor, D. A. R. Dalvit, M. Sykora, H.-T. Chen, *Nano Lett.* **2018**, *18*, 7665.

[13] M. Chirumamilla, G. V. Krishnamurthy, K. Knopp, T. Krekeler, M. Graf, D. Jalas, M. Ritter, M. Störmer, A. Y. Petrov, M. Eich, *Sci. Rep.* **2019**, *9*, https://doi.org/10.1038/s41598-019-43640-6.

[14] R. Bhatt, I. Kravchenko, M. Gupta, *Sol. Energy* **2020**, *197*, 538.

[15] J. H. Kim, S. M. Jung, M. W. Shin, *Opt. Express* **2019**, *27*, 3039.

[16] K. Cui, P. Lemaire, H. Zhao, T. Savas, G. Parsons, A. J. Hart, *Adv. Energy Mater.* **2018**, *8*, 1801471.

[17] V. Rinnerbauer, A. Lenert, D. M. Bierman, Y. X. Yeng, W. R. Chan, R. D. Geil, J. J. Senkevich, J. D. Joannopoulos, E. N. Wang, M. Soljacic, I. Celanovic, *Adv. Energy Mater.* **2014**, *4*, 1400334.

[18] V. Rinnerbauer, S. Ndao, Y. X. Yeng, W. R. Chan, J. J. Senkevich, J. D. Joannopoulos, M. Soljačić, I. Celanovic, *Energy Environ. Sci.* **2012**, *5*, 8815.

[19] W. R. Chan, V. Stelmakh, M. Ghebrebrhan, M. Soljacic, J. D. Joannopoulos, I. Celanovic, *Energy Environ. Sci.* **2017**, *10*, 1367.

[20] V. Rinnerbauer, Y. X. Yeng, W. R. Chan, J. J. Senkevich, J. D. Joannopoulos, M. Soljacic, I. Celanovic, *Opt. Express* **2013**, *21*, 11482.

[21] M. Garín, D. Hernández, T. Trifonov, R. Alcubilla, *Sol. Energy Mater. Sol. Cells* **2015**, *134*, 22.

[22] A. Kohiyama, M. Shimizu, H. Yugami, *Appl. Phys. Express* **2016**, *9*, 112302.

[23] A. Lenert, D. M. Bierman, Y. Nam, W. R. Chan, I. Celanovic, M. Soljacic, E. N. Wang, *Nat. Nanotechnol.* **2014**, *9*, 126.

[24] W. R. Chan, P. Bermel, R. C. N. Pilawa-Podgurski, C. H. Marton, K. F. Jensen, J. J. Senkevich, J. D. Joannopoulos, M. Soljacic, I. Celanovic, *Proc. Natl. Acad. Sci. U.S.A.* **2013**, *110*, 5309.

[25] A. Chirumamilla, Y. Yang, M. H. Salazar, F. Ding, D. Wang, P. K. Kristensen, P. Fojan, S. I. Bozhevolnyi, D. S. Sutherland, K. Pedersen, M. Chirumamilla, *Mater. Today Phys.* **2021**, *21*, 100503.

[26] G. Vaidhyanathan Krishnamurthy, M. Chirumamilla, T. Krekeler, M. Ritter, R. Raudsepp, M. Schieda, T. Klassen, K. Pedersen, A. Y. Petrov, M. Eich, M. Störmer, *Adv. Mater.* **2023**, *35*, 2305922.

[27] T. Krekeler, S. S. Rout, G. V. Krishnamurthy, M. Störmer, M. Arya, A. Ganguly, D. S. Sutherland, S. I. Bozhevolnyi, M. Ritter, K. Pedersen, A. Y. Petrov, M. Eich, M. Chirumamilla, *Adv. Opt. Mater.* **2021**, *9*, 2100323.

[28] M. Chirumamilla, G. V. Krishnamurthy, S. S. Rout, M. Ritter, M. Störmer, A. Y. Petrov, M. Eich, *Sci. Rep.* **2020**, *10*, 3605.

[29] K. A. Arpin, M. D. Losego, A. N. Cloud, H. Ning, J. Mallek, N. P. Sergeant, L. Zhu, Z. Yu, B. Kalanyan, G. N. Parsons, G. S. Girolami, J. R. Abelson, S. Fan, P. V. Braun, *Nat. Commun.* **2013**, *4*, 2630.

[30] M. P. Wells, R. Bower, R. Kilmurray, B. Zou, A. P. Mihai, G. Gobalakrichenane, N. M. Alford, R. F. M. Oulton, L. F. Cohen, S. A. Maier, A. V. Zayats, P. K. Petrov, *Opt. Express* **2018**, *26*, 15726.

[31] H.-J. Lee, K. Smyth, S. Bathurst, J. Chou, M. Ghebrebrhan, J. Joannopoulos, N. Saka, S.-G. Kim, *Appl. Phys. Lett.* **2013**, *102*, 241904.

[32] G. V. Krishnamurthy, M. Chirumamilla, S. S. Rout, K. P. Furlan, T. Krekeler, M. Ritter, H.-W. Becker, A. Y. Petrov, M. Eich, M. Störmer, *Sci. Rep.* **2021**, *11*, 3330.

[33] P. M. Volyles, D. A. Muller, J. L. Grazul, P. H. Citrin, H.-JL. Gossmann, *Nature.* **2002**, *416*, 826.

[34] R. Erni, H. Heinrich, G. Z. Kostorz ETH, *Ultramicroscopy* **2003**, *94*, 125.

[35] D. O. Klenov, S. Stemmer, *Ultramicroscopy* **2006**, *106*, 889.

[36] T. Bauer, Photovoltaic Cells, in, *Thermophotovoltaics. Green Energy and Technology*, Springer, Berlin, Heidelberg **2011**, *7*, https://doi.org/10.1007/978-3-642-19965-3.

[37] L. Tang, L. M. Fraas, Z. Liu, C. Xu, X. Chen, *IEEE Trans. Electron Devices* **2015**, *62*, 2809.

[38] D. L. Chubb, A. T. Pal, M. O. Patton, P. P. Jenkins, *J. of the European Ceramic Society* **1999**, *19*, 2551.

[39] E. S. Sakr, Z. Zhou, P. Bermel, *Appl. Phys. Lett.* **2014**, *105*, 111107.

[40] Q. Su, D. Yoon, A. Chen, F. Khatkhatay, A. Manthiram, H. Wang, *J. Power Sources* **2013**, *242*, 455.

[41] S. Cho, J. Yoon, J.-H. Kim, X. Zhang, A. Manthiram, H. Wang, *J. Mater. Res.* **2011**, *26*, 854.

[42] V. Singhal, J. Zhu, J. Song, H. Wang, P. Bermel, *Appl. Phys. Lett.* **2023**, *123*, 131101.